

Structured Low-Rank Algorithms

Theory, magnetic resonance applications, and links to machine learning



©ISTOCKPHOTO.COM/GOODLIFE STUDIO

In this article, we provide a detailed review of recent advances in the recovery of continuous-domain multidimensional signals from their few nonuniform (multichannel) measurements using structured low-rank (SLR) matrix completion formulation. This framework is centered on the fundamental duality between the compactness (e.g., sparsity) of the continuous signal and the rank of a structured matrix, whose entries are functions of the signal. This property enables the reformulation of the signal recovery as an SLR matrix completion problem, which includes performance guarantees. We also review fast algorithms that are comparable in complexity to current compressed sensing (CS) methods, which enable the framework's application to large-scale magnetic resonance (MR) recovery problems. The remarkable flexibility of the formulation can be used to exploit signal properties that are difficult to capture by current sparse and low-rank optimization strategies. We demonstrate the utility of the framework in a wide range of MR imaging (MRI) applications, including highly accelerated imaging, calibration-free acquisition, MR artifact correction, and ungated dynamic MRI.

Introduction

The slow nature of signal acquisition in MRI, where the image is formed from a sequence of Fourier samples, often restricts the achievable spatial and temporal resolution in multidimensional static and dynamic imaging applications. Discrete CS methods have provided a major breakthrough that accelerate the MR signal acquisition by reducing the sampling burden. As described in an article in this issue of *IEEE Signal Processing Magazine* [1], these algorithms utilize the sparsity of the discrete signal in a transform domain to recover the images from a few measurements.

In this article, we review a continuous-domain extension of CS using an SLR framework for the recovery of an image or a series of images from a few measurements using various compactness assumptions [2]–[22]. The general strategy of the SLR framework begins with defining a lifting operation that constructs a structured matrix, whose entries are functions of the signal samples. SLR algorithms capitalize on the dual

relationships between the signal compactness properties (e.g., sparsity and smoothness) and the rank of the lifted matrix. This dual relationship allows for the recovery of the signal from a few samples in the measurement domain as an SLR optimization problem. Although this strategy may seem contrived, the main benefit of this framework is its remarkable flexibility in exploiting the compactness properties of a variety of signal structures, including continuous-domain real-world signals that classical approaches have difficulty capturing. For example, SLR approaches can recover continuous-domain images from a few Fourier measurements with minimal discretization errors, unlike CS approaches. SLR methods can account for signals with an infinite number of signal discontinuities that are localized to a curve/surface, which is more a general setting than signals with a finite number of isolated signal discontinuities considered in recent superresolution methods [23]. In addition, SLR schemes contain fast algorithms that are readily applicable to large-scale imaging applications such as static and dynamic MRI, unlike superresolution methods [23], which rely on semidefinite programming. Another example of SLR methods is the recovery of images from their multichannel measurements with unknown sensitivities [5], [9], [13], [18]. These schemes depend on the low-rank structure of a structured matrix obtained by concatenating block Hankel matrices, which are acquired from each channel image. It is difficult for classical convex CS algorithms to exploit such complex relations between multichannel measurements. Also, SLR schemes have recently been extended to recover an ensemble of images that lie on a smooth surface in high-dimensional space. The current subspace model or a union of a subspace model is not efficient in capturing the aforementioned property; rather, inspired by kernel methods [24], one can define a nonlinear mapping that will transform the smooth surface to a subspace. In SLR approaches, this structure can be exploited by the construction of a structured matrix, whose columns are nonlinearly transformed signal samples.

The SLR framework is closely related to extensive work on linear predictions in MRI, which was often formulated using an SLR matrix [2]–[4], [6], [7]. Early work dates to 1985 in the context of MR spectroscopy [2], followed by its generalization to MRI by modeling the images as piecewise 1D polynomials by Liang et al. [3]. The finite rate of innovation (FRI) theory [25] also considers the recovery of piecewise polynomials and similar models from a finite number of samples. Multichannel linear-predictive relations were introduced in the parallel MRI context in [4] and [6], while linear-predictive k -space relations resulting from support and phase constraints were introduced in [7]. The reader is referred to [22], which is focused on a more elaborate review of linear prediction approaches and their history in the MRI context. Recent developments in low-rank structured matrix approaches for MRI are as follows:

- The early 1D approaches [3], [25], are generalized to multidimensional continuous-domain signals [7], [9], [10]. Theoretical guarantees are also available for multidimensional signals, whose discontinuities are localized to sets of

infinite size but of zero Lebesgue measure (e.g., curves in 2D and surfaces in 3D) [10].

- Low-rank matrix-recovery algorithms with recovery guarantees are used to recover signals from nonuniform measurements [7], [9], [15], as opposed to the explicit annihilating filter estimation from the uniform sampling setting in the classical FRI [3], [25]. Note that an earlier work in this respect goes back to the work by Dologlou et al. [26].
- The framework is generalized to the recovery of signals from nonuniform multichannel measurements with unknown channel responses, which facilitate the reduction in samples and calibration-free recovery in a unified matrix completion framework [5], [6], [9], [13], [18].
- The nonlinear generalization of FRI theory enables the recovery of points on smooth surfaces in high-dimensional spaces, which facilitates the joint reconstruction of an ensemble of images from their few measurements [21].
- The main practical benefit of SLR schemes is their ability to capture a broad range of signal priors, resulting in a wide range of applications, including static MRI [5], [7], [9], [15], [16], dynamic MRI, diffusion MRI (DMRI) [18], MR artifact correction [17], parallel MRI [5], [6], [9], multicontrast image recovery [19], spectroscopic imaging [11], [27], and field inhomogeneity compensation [28], [29].

These generalizations are accompanied by theoretical recovery guarantees [14], [16], and fast algorithms [9], [15]. Moreover, this framework provides rich insights into the deep links between 1D FRI sampling theory [25], CS [30], LR matrix completion, and superresolution theory [23].

Overview

Image acquisition in MRI

In this section, we briefly describe image formation in MRI and introduce notations and terminologies used throughout the article.

Single-channel MRI measurements

The image acquisition in MRI constitutes the sampling of the Fourier transform of the image $f(\mathbf{x})$. The measurements in the Fourier domain (referred to as k -space) are denoted by

$$\hat{f}(\mathbf{k}) = [\mathcal{F}f](\mathbf{k}) := \int f(\mathbf{x}) e^{-i2\pi\mathbf{k}^T\mathbf{x}} d\mathbf{x}. \quad (1)$$

Here, $\mathbf{x} \in \mathbb{R}^d$, $d = 2, \dots, 4$ and $\mathbf{k} \in \mathbb{Z}^d$ represent the image domain and k -space coordinates, respectively. The goal of MR image recovery, then, is to reconstruct $f(\mathbf{x})$ from these measurements, which are measured on a sparse subset of the Fourier domain.

Multichannel measurements

Modern scanners acquire the Fourier domain data using multiple receive coils to accelerate the acquisition. These receive coils have different spatial sensitivity patterns, thus providing complementary information. The measurement from the i th coil is the Fourier transform of the coil-sensitivity weighted image and is denoted by

$$\hat{f}_i(\mathbf{k}) = [\mathcal{F}f_i](\mathbf{k}), \text{ where } f_i(\mathbf{x}) = s_i(\mathbf{x})f(\mathbf{x}); i = 1, \dots, N_c. \quad (2)$$

Here, $s_i(\mathbf{x})$ denotes coil sensitivities, $f_i(\mathbf{x})$ is the coil-sensitivity weighted image, and N_c is the number of receive coils. The goal of parallel MR image recovery is to reconstruct $f(\mathbf{x})$ from a few measurements with or without the knowledge of the coil sensitivities.

Although the term *multichannel measurements* typically implies the multicoil measurements described previously, we will use the term in a broader sense. As discussed later in this article, different k -space regions are often acquired with slightly different acquisition conditions in MRI. The distortions can often be modeled as spatial weighting terms, similar to coil sensitivities. For example, the signals corresponding to the odd-only and even-only lines of k -space often differ in phase errors; we consider it a two-channel acquisition with unknown spatial weighting terms.

SLR methods: Bird's-eye view

The SLR framework offers a versatile toolbox that exploits a variety of properties of continuous-domain multichannel signals without the need for discretization. SLR algorithms rely on a “lifting” of the original signal to a matrix (see Figure 1); the structure of this matrix depends on the specific signal properties (e.g., continuous-domain sparsity and multichannel relations). The framework relies on the dual relationship between the compactness of the signal (e.g., sparsity) and the rank of the lifted matrix.

Interpolation via structured low-rank matrix completion

In several accelerated MRI acquisitions, the measurements from the full k -space locations are not available. When the signal samples are acquired in a nonuniform fashion, one can rely

on a structured low-rank matrix completion to interpolate the missing entries in the lifted matrix. Specifically, this entails determining a matrix with the lowest rank that preserves the structure of the lifted matrix and is consistent with the measured matrix entries. Once the matrix is completed, inverse lifting is performed to recover the samples of the continuous-domain signal. We term this class of methods *interpolation schemes* [5], [7], [9], [15].

Extrapolation using two-step SLR algorithms

In some applications, a certain limited region of k -space is acquired without any undersampling (usually referred to as the *calibration region*, typically in the low-frequency regions). The superresolution approaches in signal processing [23] aim to extrapolate these Fourier coefficients to high-frequency regions, thus recovering the images at higher resolution. The SLR extrapolation strategy is to estimate the null space of the lifted matrix from the fully sampled rows (indicated by the red boxes in Figure 1(b)). Given the null-space filters, it is possible to 1) estimate a signal model based on the roots of the null-space filters, followed by a linear estimation of the unknown signal model parameters or 2) perform a linear prediction to extrapolate the high-frequency samples from the measured ones subject to the null-space constraints [3], [4], [10].

Signal extrapolation using SLR

We now focus on specific continuous-domain signal models and reveal their connection to the lifted matrices that facilitate the recovery of the continuous-domain signal. In this section, we present the SLR extrapolation where the low-frequency Fourier region is fully sampled, as depicted in Figure 1(b).

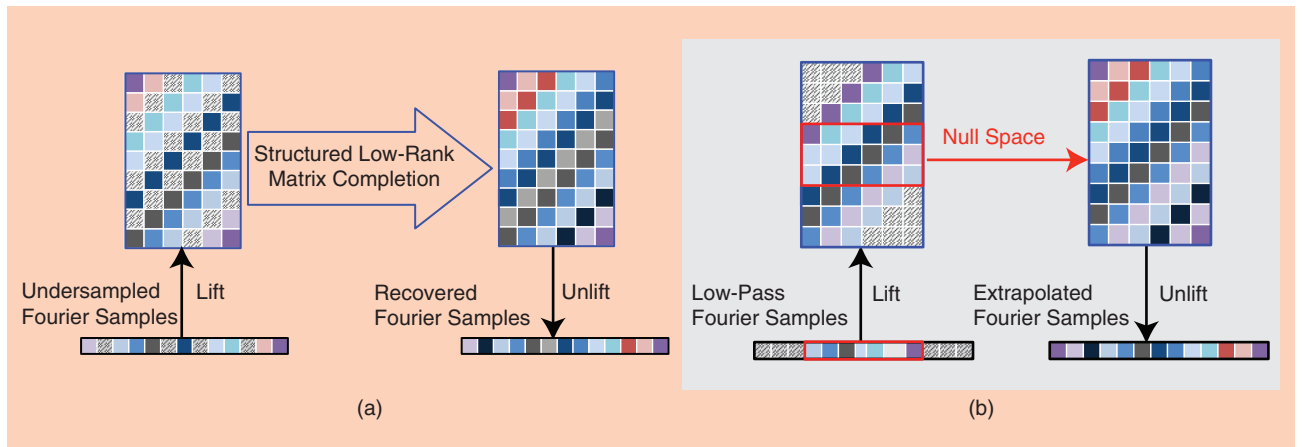


FIGURE 1. An illustration of SLR-based interpolation and extrapolation methods in the context of 1D FRI. (a) In SLR interpolation, the data are acquired on a nonuniformly subsampled Fourier grid. The SLR interpolation scheme relies on a lifting of the signal samples to a Hankel matrix, which has missing entries indicated by the hashed boxes. The one-to-one relation between the rank of a matrix and the continuous domain sparsity of the space domain signal is used to pose the recovery of missing samples as a structured low-rank matrix completion problem in the lifted matrix domain. Specifically, the algorithm determines the matrix with the lowest rank that satisfies the Hankel structure and is consistent with the known matrix entries. Postrecovery, the matrix is unlifted to obtain the Fourier samples of the signal. (b) In SLR extrapolation problems, the low-frequency Fourier coefficients of the signal are uniformly sampled. The central fully known matrix region is used to estimate the null space of the matrix, which is used to perform a linear prediction/extrapolate the missing high-frequency samples. The SLR algorithms that exploit the different signal structures differ only in the structure of the lifted matrix; the algorithms are essentially the same.

FRI theory for piecewise, smooth 1D signals

This approach [2], [3], [25] is a generalization of Prony's method of continuous-domain 1D signals. Consider the recovery of r -stream of Diracs f [see Figure 2(a)] at locations x_j , $j = 1, \dots, r$ with weights w_j :

$$f(x) = \sum_{j=1}^r w_j \delta(x - x_j), \quad x_j \in [0, 1]. \quad (3)$$

The discrete Fourier transform of this continuous-domain signal is a linear combination of complex exponentials with frequencies $\alpha_j = e^{-i2\pi x_j}$, specified by

$$\hat{f}[k] = \sum_{j=1}^r w_j (\alpha_j)^k, \quad \forall k. \quad (4)$$

The classical Prony's results [25] rely on the annihilation of such exponential signals by

$$\hat{h}(z) = \prod_{j=1}^r (1 - \alpha_j z^{-1}) = \sum_{n=0}^r h[n] z^{-n}, \quad (5)$$

such that the associated $(r+1)$ -tap filter $\hat{h}[n]$ annihilates the Fourier samples \hat{f} :

$$(h * \hat{f})[k] = 0, \quad \forall k. \quad (6)$$

This linear convolution relation (6) can be re-expressed in the matrix form (see Figure 1) to solve for \hat{h} :

$$\underbrace{\begin{bmatrix} \hat{f}[0] & \hat{f}[1] & \dots & \hat{f}[r] \\ \hat{f}[1] & \hat{f}[2] & \dots & \hat{f}[r+1] \\ \vdots & \vdots & \ddots & \vdots \\ \hat{f}[r-1] & \dots & \hat{f}[2r-1] \end{bmatrix}}_{\mathbf{H}_{[r+1]}^{[2r]}(\hat{f})} \underbrace{\begin{bmatrix} h[r] \\ \vdots \\ h[0] \end{bmatrix}}_{\mathbf{h}} = 0. \quad (7)$$

Here, the notation $\mathbf{H}_{[r+1]}^{[2r]}(\hat{f})$ represents the linear convolution matrix, which is defined for the $2r$ samples of \hat{f} to be convolved with a filter of size $r+1$; here $[r]$ denotes the set $0, 1, \dots, r$. Note that $\mathbf{H}_{[r+1]}^{[2r]}(\hat{f})$ is a Hankel-structured matrix and that the matrix lifting thus originates from the linear convolution embedded in (6) and (7) and is illustrated in Figure 1. The relation (7) can be used to identify \mathbf{h} . Once this linear-prediction filter \mathbf{h} is available, the linear-predictive relations (6) can be used to extrapolate the signal samples $\hat{f}[k]$; $k = 0, \dots, 2r-1$ to any extent in Fourier space.

Theoretical guarantees

Based on (7), filter \mathbf{h} can be estimated as a null-space vector of the lifted matrix, as shown in Figure 1(b). If $2r$ signal consecutive samples are available, the null-space vector is unique [3], [25]. Note that, from (5), the roots/zeros of $\hat{h}(z)$ will specify α_j in (4). One can then solve a system of equations with r unknowns to recover the w_j in (3); this estimation is unique with $2r$ measurements.

Spatial-annihilation relations

The results discussed in the previous section can be generalized to recover piecewise constant signal f [see Figure 2(a)], with r discontinuities located at t_j ; $j = 1, \dots, r$. The derivative

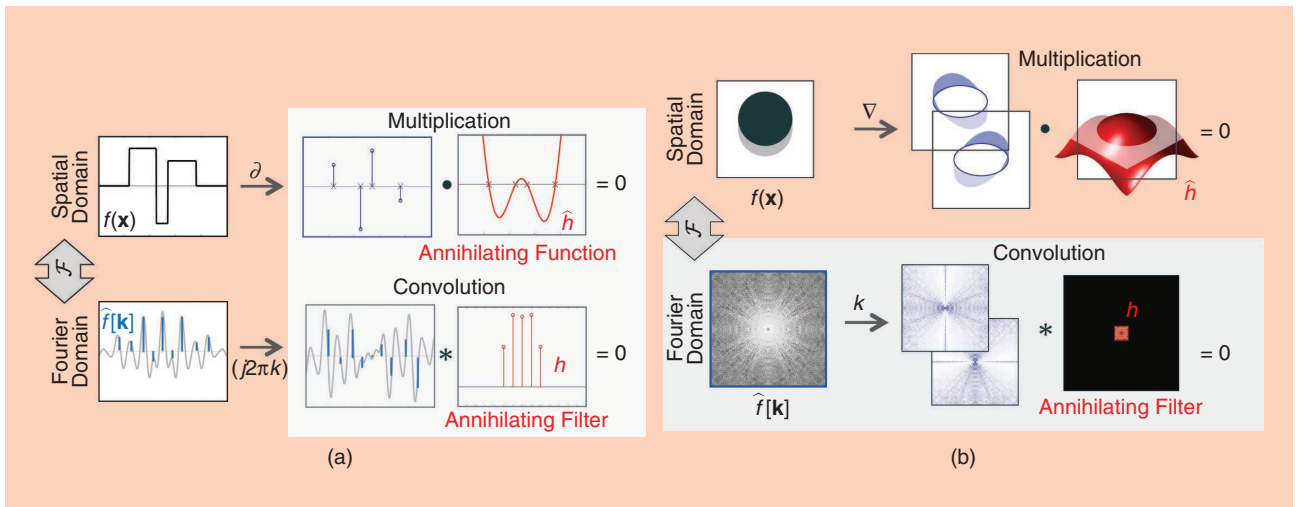


FIGURE 2. An illustration of 1D and 2D FRI relations. (a) We illustrate Prony's results in the white box, which demonstrates the recovery of Diracs at arbitrary locations. The Fourier coefficients of this signal consist of complex exponentials denoted by $\hat{f}[\mathbf{k}]$ in the bottom row. Prony's results show that complex exponentials can be annihilated by the convolution with a filter h . This Fourier domain convolution relation can also be viewed as a multiplication-based annihilation relation in the space domain. These results can be extended to the recovery of piecewise constant 1D signals by considering the derivative. Specifically, the derivative of piecewise constant signals consists of a linear combination of Diracs, which brings the problem to Prony's setting. (b) An extension of 1D FRI to the 2D setting. The gradient of the piecewise constant signal consists of a series of Diracs supported on curves and the location of image edges. We observe that the gradient can be annihilated by the multiplication by a function \hat{h} , whose zeros overlap with the image edges. If the \hat{h} is band limited, the convolution with the Fourier coefficients of the image with the filter coefficients will also be zero. We generalize the notion of 1D sparsity in FRI with the bandwidth of \hat{h} ; a more band-limited \hat{h} will correspond to smoother curves, as shown in [10]. The previously mentioned framework can be used to recover continuous-domain piecewise constant images, whose edges are localized to band-limited zero-measure curves of infinite support. This simple piecewise constant model is extended to more general piecewise smooth models in [20].

of the signal, denoted by ∂f , is a periodic stream of Diracs, as in (3). The aforementioned theory can be adapted to this setting by considering the Fourier coefficients of the derivative of $f(x)$ as, displayed in Figure 2(a). The Fourier domain convolution-based annihilation relations can also be viewed as space-domain, multiplication-based annihilation relation

$$\partial f(x) \cdot \hat{h}(x) = 0, \quad (8)$$

as shown in Figure 2(a). Here, the space-domain function $\hat{h}(x)$ is the Fourier transform of the filter $h[n]$ that annihilates the Fourier coefficients of f . The zeros of \hat{h} overlap with the location of Diracs or the location of the discontinuities of the piecewise constant signal [3]. We now use this spatial domain annihilation relations to extend the 1D results to higher dimensions.

Piecewise smooth signals in higher dimensions

In this section, we discuss how to extend the classical 1D FRI theory to recover the piecewise constant images $f(\mathbf{x})$, as depicted in Figure 2(b). We assume that the Fourier samples are available in a rectangular region $\Gamma \subset \mathbb{Z}^2$ [10]. Note that the edges of f consist of a set of curves, denoted by \mathcal{C} . To extend the space-domain annihilation relation in (8), we can assume the edge locations of the image to be represented by the zero-level sets of a 2D band-limited function, \hat{h} [10]:

$$\mathcal{C} = \{\mathbf{x} | \hat{h}(\mathbf{x}) = 0\}, \quad (9)$$

where

$$\hat{h}(\mathbf{x}) = \sum_{\mathbf{k} \in \Lambda} h[\mathbf{k}] \exp(i\mathbf{k}^T \mathbf{x}), \quad (10)$$

is bandlimited to a rectangular region $\Lambda \subset \mathbb{Z}^2$. The bandwidth of \hat{h} , denoted by $|\Lambda|$, is a measure of the complexity of the edge set [10], [31], which generalizes the notion of sparsity in compressive sensing.

Similar to (8), we have space-domain annihilation relation [see Figure 2(b)] specified by $\nabla f \cdot \hat{h} = 0$; the Fourier transform of this relation provides the 2D Fourier domain annihilation relations similar to (6):

$$\sum_{\mathbf{k} \in \Lambda} \widehat{\nabla f}[\ell - \mathbf{k}] h[\mathbf{k}] = 0, \quad \forall \ell \in \Gamma \ominus \Lambda. \quad (11)$$

Here, Γ is the set of Fourier measurements of f . Note that the convolution of $\widehat{\nabla f}$ with h at a location, \mathbf{k} , requires the samples of $\widehat{\nabla f}$ within the set $\mathbf{k} + \Lambda$, where the addition amounts to the translation of set Λ to location \mathbf{k} . Because we have only the Fourier samples of f within Γ , the convolutions specified by (6) can only be evaluated within the set $\Gamma \ominus \Lambda$, which is the morphological erosion of the set Γ by Λ . Similar to (7), the convolution relation in (11) can be rewritten in the matrix form similar to (7) as

$$\begin{bmatrix} \mathbf{H}_\Lambda^\Gamma(i\omega_x \hat{f}) \\ \mathbf{H}_\Lambda^\Gamma(i\omega_y \hat{f}) \end{bmatrix} \mathbf{h} = 0, \quad (12)$$

$\mathbf{V}_\Lambda^\Gamma(\hat{f})$

where \mathbf{h} represents the vectorized filter coefficients. Here, $\mathbf{H}_\Lambda^\Gamma(i\omega_x \hat{f})$ is the matrix corresponding to the 2D convolution of $i\omega_x \hat{f}$, and $\mathbf{V}_\Lambda^\Gamma(\hat{f})$ is a composite matrix obtained by stacking the block Hankel matrices vertically, as shown in Figure 3(a).

Theoretical guarantees

Filter \mathbf{h} and, equivalently, the edges of f , can be estimated from (12) as the null-space vector of $\mathbf{V}_\Lambda^\Gamma(\hat{f})$. It is presented in [10, Th. 1] that, $\mathbf{V}_\Lambda^\Gamma(\hat{f})$ will have a unique null-space vector when the uniform Fourier samples of \hat{f} are available within 3Λ , which is the three-fold dilation of Λ . The piecewise constant signal will then be uniquely identified from its Fourier measurements within 3Λ [10, Th. 4].

Note that the piecewise constant signal model in this section assumes a finite or infinite number of signal discontinuities supported on a set of zero measure. This framework is more general than [23], which assumes a finite number of isolated discontinuities. We note that, even more-general continuous-domain models [7], which assume the signal support to be a region of nonzero measure, do exist. Because these models have infinite degrees of freedom, it is difficult to guarantee the recovery of such a signal from finite measurements.

Exponential 1D signals

The recovery of exponentially decaying signals are important to MRI because the temporal evolution of MRI signals in the presence of chemical shifts, field inhomogeneity, and multiple relaxation mechanisms can be modeled as a linear combination of exponentials [2], [11], [27]. Specifically, the 1D exponential signal at spatial location \mathbf{x} that evolves as a function of time can be expressed as

$$f(\mathbf{x}, t) = \sum_{j=1}^r a_j(\mathbf{x}) (\beta_j(\mathbf{x}))^t; \quad t = 1, \dots, T, \quad (13)$$

where the goal is to estimate the exponential parameters from their time series. Because the relation in (5) is true for the signal model in (13), Hankel matrices $\mathbf{H}_{[r]}^{[n]}(\hat{f}_{\mathbf{x}})$ of the form (7) of each pixel at location \mathbf{x} , analogous to the description in the ‘‘FRI Theory for Piecewise, Smooth 1D Signals’’ section, can be built. Following (4)–(7), these matrices will have a null-space vector parameterized by the exponential parameters. The roots of the null-space vector are estimated using singular value decomposition (SVD), which is used to identify the exponential parameters. These subspace strategies based on the SVD of $\mathbf{H}_{[r]}^{[n]}(\hat{f}_{\mathbf{x}})$ is widely used in the context of MR spectroscopy [2], [11], [27].

Signal interpolation using SLR

This section explains how the extrapolation-based approaches discussed in the previous section can be extended to the nonuniform setting. As shown in Figure 1, we make use of the duality between the rank of the lifted matrices and the compactness priors to fill in the missing entries. Note that such sampling patterns are of high relevance in CS applications. The generalization of SLR can be accomplished using theoretical performance guarantees, which are similar to those of standard CS approaches [30].

Piecewise, smooth 1D signals

Consider the signal model displayed in the “FRI Theory for Piecewise, Smooth 1D Signals” section with r Diracs. For a Hankel structured matrix $\mathbf{H}_{[d]}^{[n]}(\hat{f}) \in \mathbb{C}^{(n-d) \times d}$ with $d > r$, the authors in [14]

$$\text{rank}(\mathbf{H}_{[d]}^{[n]}(\hat{f})) = r. \quad (14)$$

A similar observation was made in early work [3]. The authors in [14] further showed that (14) is applicable for general FRI signals with the minimum annihilating filter size of $r + 1$ on its spectral domain. This property is useful for recovering sparse signals from Fourier measurements. Specifically, let χ be a multiset consisting of random indices from $\{0, \dots, n-1\}$, such that $|\chi| = m < n$. Then, as depicted in Figure 1(a), we can interpolate $\hat{f}[k]$ for all $k \in \{0, \dots, n-1\}$ from the sparse Fourier samples utilizing (14) as:

$$\underset{\hat{g} \in \mathbb{C}^n}{\text{minimize}} \|\mathbf{H}_{[d]}^{[n]}(\hat{g})\|_* \quad \text{subject to } P_\chi(\hat{g}) = P_\chi(\hat{f}). \quad (15)$$

where $\|\cdot\|_*$ denotes the matrix nuclear norm. Here, P_χ denotes a projection operation to the set χ . Instead of using the nuclear norm, a similar problem was solved by the nonconvex optimization method [7], [26].

Theoretical guarantees

If the sampling pattern satisfies the incoherence condition with parameter ρ , then, there exists a constant c such that \hat{f} is the

unique minimizer to (15) with probability $1 - 1/n^2$ [14], provided that

$$|\chi| \geq c \rho r \log^\alpha n, \quad (16)$$

where $\alpha = 2$ if the discontinuities are located on a uniform grid; $\alpha = 4$ for general continuous-domain signals. This suggests a near-optimal performance similar to that of discrete-domain CS approaches [30].

Piecewise, smooth multidimensional signals

We now consider the recovery of the Fourier samples of the piecewise constant image described in the “Piecewise Smooth Signals In Higher Dimensions” section on $\Gamma \subset \mathbb{Z}^2$. We consider matrices $\mathbf{V}_{\Lambda_1}^\Gamma(\hat{f})$ shown in (12), where $\Lambda \subset \Lambda_1$. It is presented in [10] that

$$r = \text{rank}(\mathbf{V}_{\Lambda_1}^\Gamma(\hat{f})) = |\Lambda_1| - |\Lambda_1 \ominus \Lambda|. \quad (17)$$

It is also shown in [10] that there is a dual relationship between the above rank and the smoothness of the edge set of the images. The low-rank structure of $\mathbf{V}_{\Lambda_1}^\Gamma$ enables the recovery of \hat{f} on Γ using SLR.

Theoretical guarantees

From the results in [16, Th. 4], we conclude that the SLR algorithm recovers the true Fourier samples $\hat{f}[\mathbf{k}]$; $\mathbf{k} \in \Gamma$ from its uniform random measurements on $\chi \subset \Gamma$ with a probability exceeding $1 - |\Gamma|^{-2}$, provided that

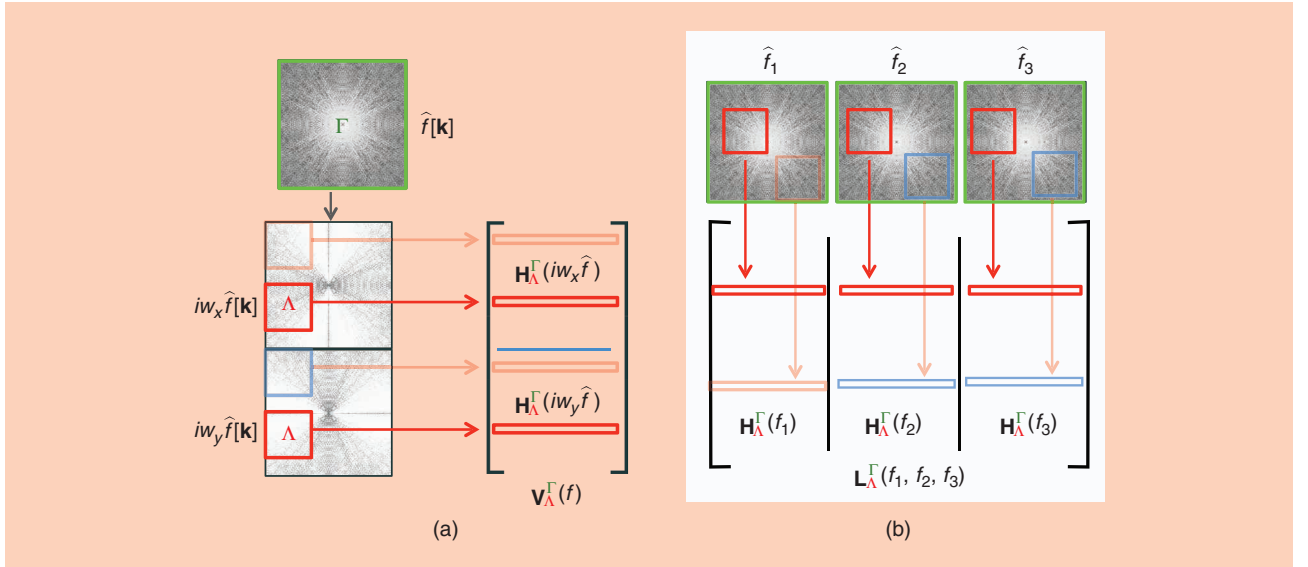


FIGURE 3. An illustration of the matrix lifting operations in 2D. (a) Vertical stacking of block Hankel matrices in (12), which is the matrix form of the convolutional relations in (11). The block Hankel matrices $\mathbf{H}_{\Lambda}^{\Gamma}(i\omega_x \hat{f})$ are constructed from the Fourier coefficients of $i\omega_x \hat{f}$. Each row of $\mathbf{H}_{\Lambda}^{\Gamma}(i\omega_x \hat{f})$ corresponds to a patch of size Λ , drawn from the Fourier coefficients supported in Γ . The number of valid shifts of Λ within Γ is denoted by $\Gamma \ominus \Lambda$ in (11). (b) Linear stacking of block Hankel matrices in (22). The block Hankel matrices of the different channels f_i are concatenated in a linear fashion to construct the composite-lifted matrix. When the low-frequency Fourier samples are fully acquired, the corresponding rows of the matrices are fully available. This facilitates the estimation of the null space from these regions, which can be used to recover the remaining k -space regions, as described in the “Signal Extrapolation Using SLR” section. When the Fourier grid is subsampled, the matrices can be completed using nuclear norm minimization, as discussed in the “Signal Interpolation Using SLR” section.

$$|\chi| \geq c \rho c_s r \log^4 |\Gamma|, \quad (18)$$

where r is defined as in (17), $c_s = |\Gamma|/|\Lambda_1|$, where c is a universal constant, and $\rho > 1$ is an incoherence measure depending on the geometry of the edge set defined in [16]. Note that the result bears remarkable similarity to (16), in the case of continuous-domain signals not on the grid.

Exponential signals with spatially smooth parameters

The approaches in the ‘‘Exponential 1D Signals’’ section examined the pixel-by-pixel recovery of exponential parameters at each spatial location \mathbf{x} from their uniform samples. The recovery of exponentials from nonuniform $k-t$ -domain samples is key to accelerating the acquisition in several MR applications. Note that the coefficients of the annihilation filters $h_s[z]$ depend on the exponential parameters at the specific pixel location \mathbf{x} . In imaging applications, the exponential parameters are often spatially smooth. The spatial Fourier transform of the filter coefficients can be assumed to be support limited to a 3D cube of size Λ . The annihilation relations can therefore be compactly expressed as

$$\mathbf{H}_\Lambda^\Gamma(\hat{f}) \mathbf{h} = 0, \quad (19)$$

where $\mathbf{H}_\Lambda^\Gamma(\hat{f})$ is the block Hankel matrix corresponding to the 3D convolution of $\hat{f}[\mathbf{k}, n]$ with filter \mathbf{h} . Similar to the discussions in the ‘‘Piecewise, Smooth 1D Signals’’ and ‘‘Piecewise, Smooth Multidimensional Signals’’ sections, matrix $\mathbf{H}_\Lambda^\Gamma(\hat{f})$ is low rank if $\Lambda \subset \Lambda_1$. Thus, the recovery of the 3D data set from its undersampled $k-t$ space measurements can be posed as an SLR problem.

Recovery of multichannel MRI data

In this section, we detail the recovery of multichannel data using calibration-based and calibration-free strategies, which are analogous to the extrapolation and interpolation methods discussed previously.

Blind multichannel deconvolution

For the blind multichannel deconvolution problems in signal processing, subspace techniques such as the eigenvector-based algorithm for multichannel blind deconvolution (EVAM) [32] utilize multichannel annihilation relations. Specifically, the multichannel measurement for blind multichannel deconvolution problems is given by $\hat{f}_i = \hat{s}_i * \hat{f}$, $i = 1, \dots, N_c$, where N_c denotes the number of channels, \hat{s}_i represents the unknown convolution kernels, and \hat{f} is the unknown underlying signal. The goal of the blind multichannel deconvolution problem is to estimate \hat{f} and \hat{s}_i from \hat{f}_i .

EVAM [32] relies on cross-channel annihilating filter relations, expressed as

$$\hat{f}_i * \hat{s}_j - \hat{f}_j * \hat{s}_i = 0, \quad \forall i \neq j. \quad (20)$$

Assuming that the convolution kernel \hat{s}_j can be represented by the d -tap filter, the previously mentioned convolution relations can be compactly represented in matrix form as

$$[\mathbf{H}_\Lambda^\Gamma(\hat{f}_i) | \mathbf{H}_\Lambda^\Gamma(\hat{f}_j)] \begin{bmatrix} \hat{s}_j \\ -\hat{s}_i \end{bmatrix} = 0. \quad (21)$$

We now demonstrate that the extension of this method to the MRI setting is similar to that of the popular parallel MRI schemes [5], [33], that were discovered independently without realizing this connection.

Calibration-based parallel MRI recovery

The space-domain annihilation relations $f_i(\mathbf{x}) \cdot s_j(\mathbf{x}) - f_j(\mathbf{x}) \cdot s_i(\mathbf{x}) = 0$ that correspond to (20) were used in [34]. The Fourier domain annihilation relations between each pair of channels, as in (21), implies that the matrix formed by linearly stacking the Hankel matrices of f_i , $i = 1, \dots, N_c$

$$\mathbf{L}_\Lambda^\Gamma(f_1, \dots, f_{N_c}) = [\mathbf{H}_\Lambda^\Gamma(\hat{f}_1) | \mathbf{H}_\Lambda^\Gamma(\hat{f}_2) | \mathbf{H}_\Lambda^\Gamma(\hat{f}_{N_c})], \quad (22)$$

is low rank [4]–[6], [9], [13], [18], [26].

In calibration-based parallel MRI, the central Fourier regions are often acquired in a fully sampled fashion. In this case, null-space \mathbf{V} can be estimated from the central regions, similar to the approach depicted in Figure 1(b). Once the null-space filters are available, the relation $\mathbf{L}_\Lambda^\Gamma \mathbf{V} = 0$ can be used to complete the full matrix (22) from its partial entries. Consider one column of \mathbf{V} , denoted by $\mathbf{v} = [\mathbf{w}_1^T | \mathbf{w}_2^T | \dots | \mathbf{w}_{N_c}^T]^T$; each vector \mathbf{w}_i is of dimension $|\Lambda|$. The relation $\mathbf{L}_\Lambda^\Gamma(f_1, \dots, f_{N_c}) \mathbf{v} = 0$ can thus be written as

$$\hat{f}_1 * \mathbf{w}_1 + \hat{f}_2 * \mathbf{w}_2 + \widehat{f_{N_c}} * \mathbf{w}_{N_c} = 0, \quad (23)$$

where $*$ denotes linear convolution. Equation (23) implies that the k -space sample of the first coil can be predicted as the linear combination of the nearby samples in all the channels, which is essentially the simultaneous auto calibrating and k -space estimation (SAKE) model [5], [33]. The generalized auto calibrating partially parallel acquisitions approach, which preceded SAKE [5], [6], can be viewed as an approximation of this linear prediction relation. See [13] for a more-detailed review of similar multichannel methods.

Calibrationless multichannel recovery

The aforementioned calibration-based framework is extended to the nonuniformly sampled k -space data in [5] and [6] using the SLR framework, which is analogous to the interpolation strategies discussed in the ‘‘Signal Interpolation Using SLR’’ section. The recovery can be interpreted as the rank deficiency of $\mathbf{L}_\Lambda^\Gamma(f_1, \dots, f_{N_c})$. Accordingly, [5], [9], and [13] use the following low-rank matrix completion to estimate the missing k -space data without any calibration data:

$$\begin{aligned} & \min_{\{g_1, \dots, g_{N_c}\}} \text{rank}(\mathbf{L}_\Lambda^\Gamma(g_1, \dots, g_{N_c})) \\ & \text{subject to } P_\chi(\hat{g}_i) = P_\chi(\hat{f}_i); \quad i = 1, \dots, N_c. \end{aligned}$$

To further exploit the annihilation relationship from the FRI model in addition to the multichannel annihilating relationship,

the authors in [9] solve the optimization problem (24), after the k -space weighting.

SLR recovery: Fast algorithms

In the section, we explain the algorithms in the context of a simple Hankel matrix lifting. Previous algorithms [5]–[7] relied on nonconvex rank constrained formulations:

$$\min_{\hat{g} \in \mathbb{C}^n} \|P_{\chi}(\hat{g}) - P_{\chi}(\hat{f})\|_2^2 \quad \text{such that } \text{rank}(\mathbf{H}_{[d]}^{[n]}(\hat{g})) \leq r, \quad (24)$$

where r is a predefined parameter. Here, P_{χ} denotes a projection operation to the set χ . Convex unconstrained formulations of the form

$$\min_{\hat{g} \in \mathbb{C}^n} \lambda \|\mathbf{H}_{[d]}^{[n]}(\hat{g})\|_* + \|P_{\chi}(\hat{g}) - P_{\chi}(\hat{f})\|_2^2, \quad (25)$$

where $\|\cdot\|_*$ denotes the matrix nuclear norm, and λ symbolizes the regularization parameter are recently being used in applications because of their ability to converge to global minima.

Iterative singular value shrinkage

The formulation in (25) can be solved using the singular value thresholding scheme expressed in [8]. Specifically, the algorithm alternates between lifting the original signal \hat{f} to form $\mathbf{H}(\hat{f})$, followed by singular value soft shrinkage of $\mathbf{H}(\hat{f})$ to obtain \mathbf{Q} , and unlifting \mathbf{Q} to impose the Hankel structure and enforce data consistency. One challenge with employing this scheme is its high computational complexity and memory demand, especially for multichannel recovery problems. In [5] and [7], the authors used the hard thresholding as a singular value shrinkage operation within a similar iterative optimization framework.

UV factorization

To reduce the computational cost, the authors in [9] and [35] used the following observation:

$$\|\mathbf{A}\|_* = \min_{\mathbf{U}, \mathbf{V}: \mathbf{A} = \mathbf{U}\mathbf{V}^H} \|\mathbf{U}\|_F^2 + \|\mathbf{V}\|_F^2, \quad (26)$$

to realize an SVD-free, structured rank-minimization algorithm. The nuclear norm minimization problem can be solved by replacing the nuclear norm term by (26). The constraints are enforced by using an alternating direction method of multipliers algorithm, whose complexity is determined by the rank. So, for sparse signals, a significant computation gain can be obtained.

Generic, iterative, reweighted annihilating filter algorithms

Both of the aforementioned strategies rely on the explicit lifting of the signal to the large Hankel matrix, which makes the memory demand and computational complexity of the algorithms high. The generic iterative reweighted annihilation filter (GIRAF) algorithm avoids the lifting steps altogether and

reduces the number of SVD steps; it solves the problem in the original signal domain, thus realizing an algorithm that is comparable in computational complexity to CS methods [15]. The GIRAF algorithm uses the iterative-reweighted least-squares (IRLS) [36] strategy, which majorizes the nuclear norm penalty as $\|\mathbf{A}\|_* \leq \|\mathbf{A}\mathbf{Q}\|_F^{1/2}$, where $\mathbf{Q} = (\mathbf{A}^* \mathbf{A})^{-1/4}$. The i th iteration of this algorithm updates \mathbf{Q} as $\mathbf{Q}_{i+1} = (\mathbf{H}_{[d]}^{[n]}(\hat{g})^* \mathbf{H}_{[d]}^{[n]}(\hat{g}_i))^{-1/4}$, followed by the minimization of a quadratic cost function to solve for g_{i+1} , which is derived by replacing the nuclear norm in (25) by $\|\mathbf{H}_{[d]}^{[n]}(\hat{g})\mathbf{Q}_n\|_F$. The GIRAF algorithm relies on fast Fourier transforms to evaluate the matrix vector product between $\mathbf{H}_{[d]}^{[n]}(\hat{g})$ and each column of \mathbf{Q} ; this approach makes use of the convolutional structure of $\mathbf{H}_{[d]}^{[n]}(\hat{g})$. We note that this approach does not require the creation or storage of the large structured matrix, but works directly with the signal samples of g . The MATLAB implementation of the GIRAF algorithm is available at <https://github.com/cbig-iowa/giraf>.

Algorithms for nonconvex SLR formulations

All of the algorithms in the previous section are designed for convex formulations (25). Early algorithms [5], [6] relied on successively solving

$$g_{n+1} = \min_{\hat{g} \in \mathbb{C}^n} \|P_{\chi}(\hat{g}) - P_{\chi}(\hat{f})\|_2^2 + \lambda \|\hat{g} - \mathcal{M}_r(\hat{g}_n)\|^2, \quad (27)$$

where $\mathcal{M}_r(\hat{g}_n)$ is the approximation of the n th iterate \hat{g}_n , such that $\mathbf{H}_{[d]}^{[n]}(\hat{g})$ is of rank r . Recently, the multiplicative majorization strategy in the GIRAF algorithm [15] was adapted into the low-rank modeling of local k -space neighborhoods (LORAKS) setting to realize faster algorithms.

Generalization to machine learning

Recovery of point clouds on surfaces: Nonlinear generalization of union of subspaces model

We now consider a nonlinear generalization of the FRI theory discussed previously, which will facilitate the recovery of surfaces or points living on surfaces from a few noisy samples. The main motivation is the joint recovery of an ensemble of images (e.g., images in a cardiac MRI time series) from their noisy and undersampled measurements. This approach is a nonlinear generalization of the popular union of subspaces model, which represents the images as a sparse linear combination of some basis images.

We model the surface as the zero level set of a band-limited function, as discussed in the “Piecewise, Smooth Multidimensional Signals” section. For simplicity, we explain the approach in 2D. Consider an arbitrary point \mathbf{x} on the curve $\hat{h}(\mathbf{x}) = 0$, where $h(\mathbf{x})$ is specified by (10). The space-domain annihilation relation translates to $\mathbf{c}^T \phi_{\Lambda}(\mathbf{x}) = 0$, where

$$\phi_{\Lambda}(\mathbf{x}) = [\exp(j\mathbf{k}_1^T \mathbf{x}) \quad \dots \quad \exp(j\mathbf{k}_{|\Lambda|}^T \mathbf{x})]^T \quad (28)$$

is a nonlinear mapping or lifting of a point \mathbf{x} to a high-dimensional space [21] (see Figure 4) of dimension, i.e., $|\Lambda|$. Because

this nonlinear lifting strategy is similar to the feature maps used in kernel methods [24], we term $\phi_\Lambda(\mathbf{x})$ as the feature map of point \mathbf{x} .

We now consider a set of N points on the curve, indicated by $\mathbf{x}_1, \dots, \mathbf{x}_N$. The aforementioned annihilation relations can be compactly represented as $\mathbf{c}^T \Phi_\Lambda(\mathbf{X}) = 0$, where

$$\Phi_\Lambda(\mathbf{X}) = [\phi_\Lambda(\mathbf{x}_1) \ \phi_\Lambda(\mathbf{x}_2) \ \dots \ \phi_\Lambda(\mathbf{x}_N)] \quad (29)$$

is the feature matrix of the points. The results in [21] suggest that if the number of samples exceeds a bound that depends on the complexity of the curve, it can be uniquely estimated.

We have shown in [21] that, if we choose a feature map with a bandwidth of Λ_1 such that $\Lambda \subset \Lambda_1$, the feature matrix satisfies the relation similar to (17):

$$\text{rank}(\Phi_{\Lambda_1}(\mathbf{X})) \leq |\Lambda_1| - |\Lambda_1 \ominus \Lambda|. \quad (30)$$

By generalizing the SLR approach in the ‘‘Signal Interpolation Using SLR’’ section, we recovered the samples on the curve/surface from a few measurements corrupted by noise [21] by solving the following optimization problem:

$$\underset{\mathbf{X}}{\text{minimize}} \ \lambda \|\Phi_{\Lambda_1}(\mathbf{X})\|_* + \|\mathcal{A}(\mathbf{X}) - \mathbf{b}\|^2. \quad (31)$$

We use an IRLS algorithm [36] that relies on the kernel trick [24] for recovery. Specifically, the algorithm alternates between a quadratic optimization scheme and the evaluation of the graph Laplacian matrix; the algorithm may be interpreted as the discretization of the manifold by a graph, whose connectivity is specified by the distances on the manifold/surface. Note that, unlike the approaches in the ‘‘Signal Interpolation Using SLR’’ section, this algorithm is nonconvex. Hence, the optimization problem (31) cannot be guaranteed to achieve the global minimum. Despite the lack of guarantees, the algorithm was able to yield good performance in applications, as seen in Figure 4 (and also later in Figure 8).

Relation to deep convolutional neural networks

One of the interesting aspects of the SLR approach is its relation to deep neural networks. Specifically, in the recent theory of deep convolutional framelets [37], the authors showed that a deep neural network can be interpreted as a framelet representation whose basis can be obtained from Hankel matrix decomposition. Moreover, in a recent follow-up study [38], the authors further revealed that the rectified linear unit (ReLU) plays a key role in making the representation adaptive to input by providing combinatorial basis selection.

Specifically, for a given Hankel matrix $\mathbf{H}(f)$, let us consider two matrices, i.e., Φ^\top and Ψ whose dimensions are determined such that they can be multiplied by the left and right of the Hankel matrix, respectively. Furthermore, suppose there exists matrices $\tilde{\Phi}$ and their duals $\tilde{\Psi}$ that satisfy the frame condition $\tilde{\Phi}\Phi^\top = \mathbf{I}$, $\Psi\tilde{\Psi}^\top = \mathbf{I}$, where superscript $^\top$ denotes the matrix transpose and \mathbf{I} refers to an identity matrix with appropriate size. The existence of such matrices can be trivially shown as infinite numbers of orthonormal matrices that satisfy the frame condition. In fact, the frame condition allows for an overcomplete representation. Then, it is easy to express

$$\mathbf{H}(f) = \tilde{\Phi}\mathbf{C}\tilde{\Psi}^\top, \text{ where } \mathbf{C} = \Phi^\top \mathbf{H}(f) \Psi. \quad (32)$$

One of the most interesting observations in [37] is that (32) can be equivalently represented by the following encoder and decoder convolution structures:

$$\mathbf{C} = \Phi^\top (f * \alpha(\Psi)), \quad f = (\tilde{\Phi}\mathbf{C}) * \beta(\tilde{\Psi}), \quad (33)$$

where $\alpha(\Psi)$ and $\beta(\tilde{\Psi})$ are the encoder and decoder layer multichannel convolution filters obtained by rearranging Ψ and $\tilde{\Psi}$, respectively [37]. This observation led to the findings that Φ^\top and $\tilde{\Phi}$ correspond to the pooling and unpooling layers, respectively [37].

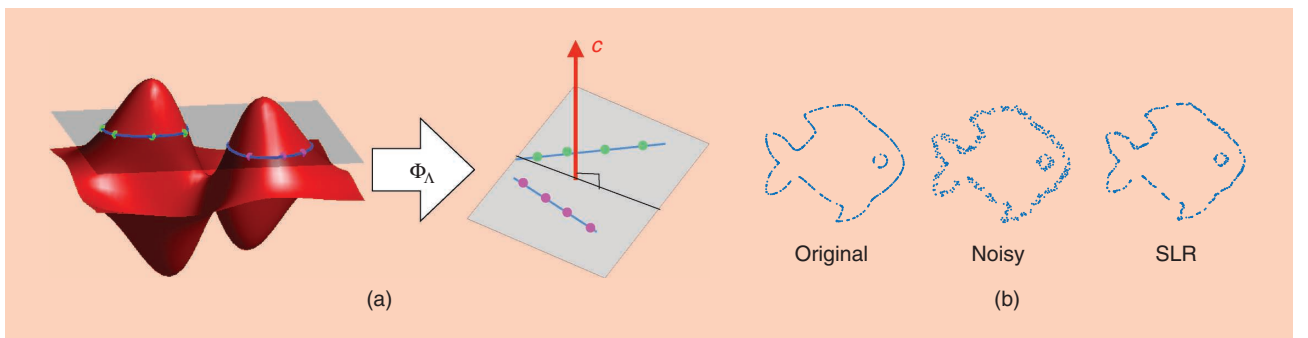


FIGURE 4. An illustration of the nonlinear lifting operation in 2D, which maps a closed union of band-limited curves to a union of subspaces. (a) Each closed curve is mapped to a subspace. The SLR scheme relies on the low-rank structure of the subspace, where the lifted points reside to recover the curves or denoise the points living on union of band-limited curves. (b) The utility of this scheme in the denoising of shapes. The recovery is posed as a nuclear norm minimization of the feature maps, which was solved using an iterative reweighted least-squares algorithm exploiting the kernel trick [21]. This approach is extended to higher dimensions to recover free-breathing and ungated cardiac MRI data, illustrated later in Figure 8.

However, to satisfy the frame conditions, the number of output filter channels should increase exponentially, which is difficult to satisfy in practice [37]. Moreover, in contrast to SLR approaches, the exact decomposition of the Hankel matrix in (33) is not interesting in neural networks because the network output should be different from the input network due to task-dependent processing. In addition, the representation should be well generalized for various inputs rather than for a specific input at the training phase. In a recent extension of the deep convolutional framelets [37], the authors revealed that the convolutional framelet representation is indeed combinatorial due to the combinatorial nature of ReLU. Specifically, for the case of an encoder–decoder convolutional neural network (CNN) without a skipped connection, it was proved that the CNN output g can be represented as follows [38]:

$$g = \sum_i \langle \mathbf{b}_i(f), f \rangle \tilde{\mathbf{b}}_i(f), \quad (34)$$

where $\mathbf{b}_i(f)$ and $\tilde{\mathbf{b}}_i(f)$ denote the i th columns of the $\mathbf{B}(f)$ and $\tilde{\mathbf{B}}(f)$ matrices given by

$$\mathbf{B}(f) = \mathbf{E}^1 \Sigma^1(f) \mathbf{E}^2 \dots \Sigma^{\kappa-1}(f) \mathbf{E}^\kappa, \quad (35)$$

$$\tilde{\mathbf{B}}(f) = \mathbf{D}^1 \tilde{\Sigma}^1(f) \mathbf{D}^2 \dots \tilde{\Sigma}^{\kappa-1}(f) \mathbf{D}^\kappa, \quad (36)$$

where $\Sigma^l(f)$ and $\tilde{\Sigma}^l(f)$ denote diagonal matrices with 0 and 1 values, which are determined by the ReLU output in the previous convolution steps; \mathbf{E}^l (respectively, \mathbf{D}^l) represents the l th layer encoder (respectively, the decoder) matrix, which is composed of pooling matrix Φ^l (respectively, the unpooling matrix $\tilde{\Phi}^l$) and encoder filter matrix Ψ^l (respectively, the decoder filter matrix $\tilde{\Psi}^l$). A similar basis representation is applicable for the encoder–decoder CNNs with skipped connections [38].

When there are no ReLU nonlinearities and when pooling and filter matrices satisfy the frame condition for each l , the representation (34) is indeed a convolutional frame representation of f , as in (33), thereby ensuring perfect signal reconstruction. Even with the ReLU, there exists conjugate filter sets that can enable perfect reconstruction conditions [37]. However, the explicit dependence of (35) and (36) on the input f due to the ReLU nonlinearity makes the neural network representation much richer and adaptive to different input signals, because the resulting frame representation in (34) is dependent on the specific input. In this regard, the role of ReLUs may be similar to that of the sparsity patterns in CS MRI because the sparsity pattern determines the different basis representations of CS for given inputs. Furthermore, the number of distinct linear representations increases exponentially with the network depth, width, and skipped connection, due to the combinatorial nature of ReLU nonlinearities [38]. This exponentially large expressivity of the neural network is another important advantage, which may, with the combination of the aforementioned adaptivity, explain the origin of the success of deep neural networks for image reconstruction.

Application of SLR for improved MRI

The main benefit of the SLR framework is its ability to account for a wide variety of signal models, thus facilitating the exploitation of extensive redundancies between their Fourier samples. This feature makes SLR applicable to a wide variety of MRI applications, which are discussed in the next section.

Highly accelerated MRI

During the past few years, various SLR priors were introduced for highly accelerated MRI, each designed to exploit specific signal properties.

Support/sparsity priors

The signal is assumed to be sparse or support limited to a region in low-rank modeling of local k -space neighborhoods (LORAKS), which results in annihilation conditions in k -space. The LORAKS scheme formulated the CS-MRI problem by using the block Hankel matrix of the images as the prior. The LORAKS framework also exploits phase constraints, which are detailed in [7].

Transform-domain sparsity

The annihilating filter-based low-rank Hankel matrix approach (also known as ALOHA) considers general signals that can also be sparse in a transform domain [3], [9], [10]. Specifically, the signal f is modeled as $\mathbf{L}f = w$, where \mathbf{L} symbolizes the following constant-coefficient linear differential equation, often called the *whitening operator* [14]:

$$\mathbf{L} := b_K \partial^K + b_{K-1} \partial^{K-1} + \dots + b_1 \partial + b_0, \quad (37)$$

and w is an innovation signal composed of a stream of Diracs or differentiated Diracs. Evaluating the Fourier transform, we achieve $\hat{w} := \hat{\mathbf{L}}\hat{f}$, where $\hat{\mathbf{L}}(f) = b_K(i2\pi f)^K + \dots + b_1(i2\pi f) + b_0$, and the associated Hankel matrix $\mathbf{H}(\hat{w})$ from the innovation spectrum \hat{w} becomes rank deficient. The Fourier coefficients are interpolated, similar to those in (15), by minimizing the nuclear norm of a block Hankel matrix, whose entries are the Fourier coefficients of \hat{f} weighted by $\hat{\mathbf{L}}$.

Piecewise smooth signal model

The GIRAF algorithm generalized the piecewise polynomial 1D model [3], [16], to recover piecewise constant multidimensional signals from their sparse Fourier coefficients by minimizing the nuclear norm of the vertically stacked block Hankel matrices in (12) [see Figure 3(a)], as described in the “Piecewise, Smooth Multidimensional Signals” section. Each of the block Hankel matrices correspond to weighted Fourier coefficients of the signal.

This model was recently extended to represent the image as a linear combination of piecewise constant (f_{pwc}) and piecewise linear components (f_{pwl}) [20]: $f(\mathbf{x}) = f_{\text{pwc}}(\mathbf{x}) + f_{\text{pwl}}(\mathbf{x})$. The recovery is posed as:

$$\min_{g_1, g_2 \in \mathbb{C}^n} \|\mathcal{T}(\widehat{\nabla g_1})\|_* + \|\mathcal{S}(\widehat{\nabla g_2})\|_* + \lambda \|P_\Omega(\hat{g}_1 + \hat{g}_2) - P_\Omega(\hat{f})\|^2,$$

where \mathcal{S} is the matrix obtained by the vertical stacking of the block Hankel matrices of three second-degree partial derivatives, denoted by the vector $\widehat{\nabla_2 f}$. We demonstrate the benefit of some of the flavors of the proposed scheme in Figure 5.

The calibration-free correction of trajectory and phase errors

The multichannel framework introduced in the “Calibration-less Multichannel Recovery” section, provides a versatile tool to solve several calibration problems in MRI, where different k -space regions are acquired from different excitations; these data sets will differ in phase errors, which often manifest as artifacts. As discussed in the “Multichannel Measurements” section, (2) can also be used to model the acquisition of multishot Fourier data. Specifically, the data are split into multiple groups or virtual channels, each corresponding to different distortions. The joint recovery of these groups or virtual channels are performed, as in (24).

Correction of phase errors in multishot DMRI

DMRI is a helpful tool for assessing brain connectivity and tissue microstructure. High-resolution DMRI is often acquired

using multishot echo-planar imaging (EPI) schemes, where different Fourier regions are acquired from different radio-frequency excitation pulses. For example, the even lines in a two-shot EPI sequence are collected from one shot, while the odd lines are collected in the second shot. Subtle physiological motion between the shots in the presence of diffusion-encoding gradients manifest as motion-induced phase errors between the shots. Previous works [18] indicate that these phase errors can be corrected using the SLR scheme, even when the data are acquired using between four and eight shots. The results in Figure 6(a) show the improved reconstructions offered by this scheme.

Compensation of trajectory errors

MRI images can also suffer from artifacts, which result from k -space data of different excitations experiencing different distortions. A typical example is radial imaging, where the shifted radial spokes cause streaking artifacts. A matrix completion using the low-rank prior [39] is used to jointly recover artifact-free images and uncorrupted calibration data. Several other groups have demonstrated the utility of the low-rank-based approach for the correction of trajectory errors in

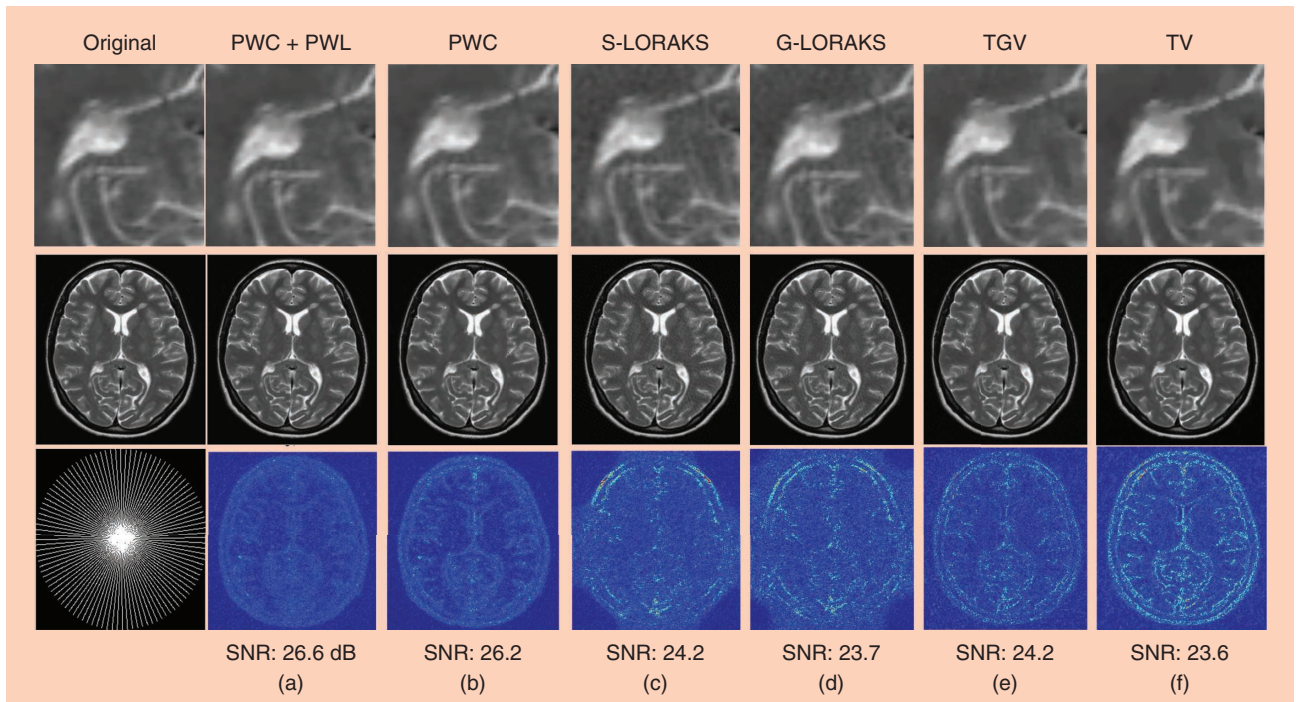


FIGURE 5. An illustration of different flavors of SLR recovery in a single-coil setting. The Fourier transform of the image was sampled on the radial grid, which corresponds to an acceleration of 4.85. The columns correspond to the following: (a) GIRAF, which assumes a piecewise constant image model, where the nuclear norm of the block Hankel matrix in (12) is minimized; (b) the generalized structured low-rank (GSLR), where the image is modeled as the sum of a piecewise constant and piecewise linear functions as in (38); (c) S-LORAKS and (d) G-LORAKS [7]; (e) total generalized variation (TGV), which is a discrete model that represents the images as the sum of piecewise linear and constant factors; and (f) total variation (TV). We note that the Fourier domain models (a) and (b) offer better reconstructions compared to their discrete counterparts (f) and (e), respectively, which can be appreciated from the zoomed images as well as the error images. We note that both (a) and (b) consider the low-rank structure of Hankel matrices constructed from weighted Fourier samples; this allows these methods to exploit the continuous sparsity of the edges, similar to discrete approaches such as TV or wavelet methods. The performance of the algorithms can be further improved by combining multiple SLR priors to exploit different signal priors (e.g., piecewise smoothness, multichannel sampling, and smoothness of phase) [18]. These combinations can be either accounted for by different regularization terms or combined into a single nuclear norm penalty of a more complex structured matrix obtained by vertical and horizontal stackings to exploit the redundancies.

EPI and radial setting (not referenced in this article due to space constraints).

Correction of k -space outliers

Many MRI artifacts from the instability of an MR system, patient motion, inhomogeneities of gradient fields, and so on are manifested as outliers in k -space data. Because MR artifacts usually appear as sparse k -space components, the artifact-corrupted MRI measurements $\hat{z}(f)$ can be modeled as $\hat{z}(f) = \hat{x}(f) + \hat{s}(f)$, where $\hat{x}(f)$ is a k -space data of an artifact-free image and $\hat{s}(f)$ is the sparse k -space outlier [17], [40]. If the unknown signal can be sparsified by applying a whitening operator (37) when performing a lifting to a Hankel-structured matrix, we can see that

$$\mathbf{H}(\hat{y}) = \underbrace{\mathbf{H}(\hat{l} \odot \hat{x})}_{\text{low-rank}} + \underbrace{\mathbf{H}(\hat{l} \odot \hat{s})}_{\text{sparse}}, \quad (38)$$

where \hat{l} denotes the spectrum of the whitening operator.

Note that the second term in (38) is sparse, because the lifted Hankel matrix from sparse components is still sparse, as illustrated in Figure 7. Thus, (38) becomes a structure for sparse

+ low-rank decomposition, and a modified version of robust principal component analysis was used to decompose the low-rank, sparse components of the Hankel matrix $\mathbf{H}(\hat{y})$. After the sparse + low-rank decomposition, the weighted k -space for the low-rank component is returned to the original k -space by performing an unweighting [17].

Recovery of exponentials

Parameter mapping

MR parameter-mapping methods [12], [19], which estimate the T_1 and T_2 relaxation constants, can enable tissue characterization and are therefore clinically very valuable. However, the long scan time resulting from the need for multiple temporal frames makes these schemes challenging for routine clinical use. The undersampling of each temporal frame, followed by sparse recovery, has been a popular approach to reduce the scan time. The spatiotemporal signal can be modeled as an exponential with smoothly varying parameters, as described in the “Exponential Signals With Spatially Smooth Parameters” section, which facilitates its recovery from undersampled measurements.

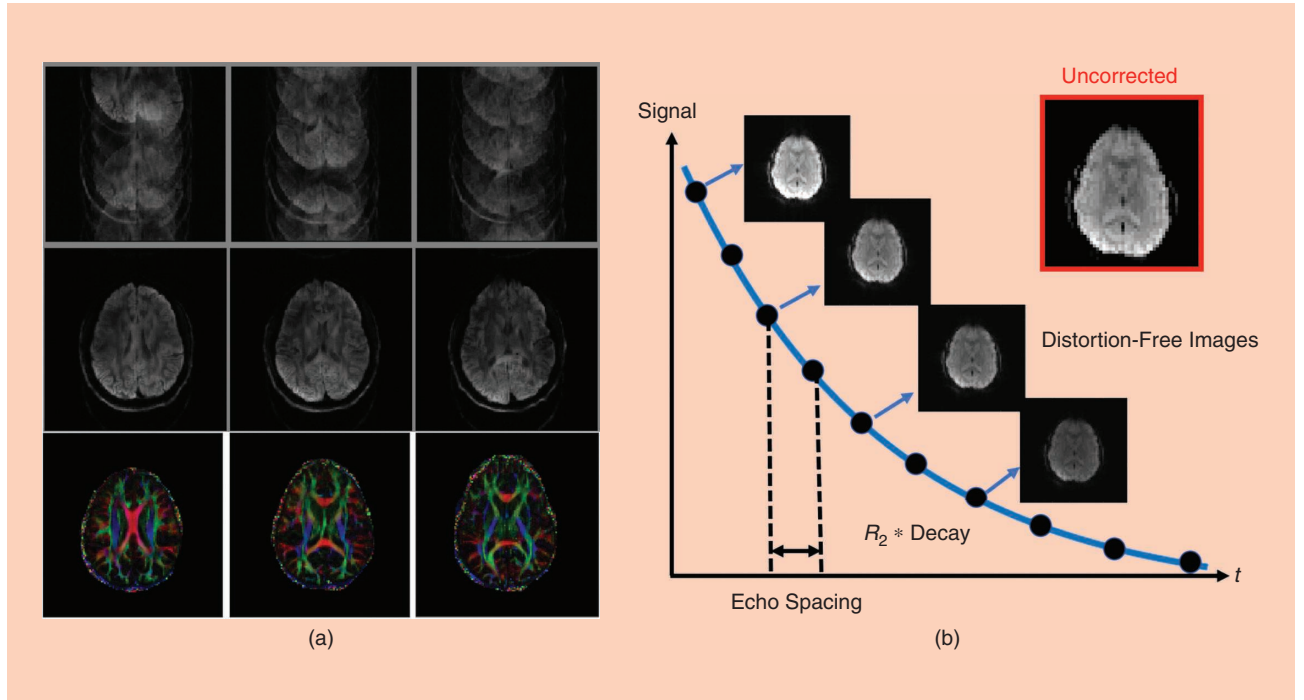


FIGURE 6. Example applications enabled by the SLR framework. (a) High-resolution four-shot diffusion MRI enabled by the SLR framework. The top row corresponds to uncorrected four-shot diffusion-weighted MRI data from a single diffusion direction. Subtle subject motion between the shots results in phase errors between the measured Fourier data sets. In addition, eddy current artifacts also manifest as shifts in Fourier space between odd/even lines. These errors manifest as Nyquist ghosting artifacts in the uncorrected diffusion-weighted images (DWI) in the top row. The SLR algorithm called *MUSSELS* [18] recovers the eight images, corresponding to each shot and odd/even lines separately, exploiting the phase relations between the images. The sum-of-squares combined DWI data from the aforementioned eight images for each slice are shown in the second row. The information from 60 such directions provides the fractional anisotropy diffusion MRI maps shown in the bottom row. (b) Correction of B0 distortions in EPI data [29]. The long readouts in EPI often result in spatial distortions, stemming from the inhomogeneity of the main (B0) magnetic field. Ignoring the B0-induced magnetization evolution during the long EPI readouts will be associated with spatial distortions. We reformulated the EPI distortion correction as a time-series recovery problem, where multiple images corresponding to different segments of the readouts are recovered, exploiting the exponential structure of the signal. Note that each of the segments is highly undersampled. The missing Fourier samples are filled in using a structured low-rank matrix completion.

Field inhomogeneity compensation

MRI schemes such EPI are associated with long readouts. The EPI signal at time point t after the excitation is the Fourier sample of the image modulated by a time-evolving exponential: $\rho[\mathbf{r}, n] = f(\mathbf{r})\beta(\mathbf{r})^n$, where the exponential parameter $\beta(\mathbf{r}) = e^{-(\mathbf{R}_2^*(\mathbf{r}) + j\omega(\mathbf{r}))T}$ results from the field inhomogeneity, and T is the sampling rate in time [28], [29]; $f(\mathbf{r})$ is the true image. The standard inverse Fourier transform reconstruction ignoring the exponential term thus recovers the field inhomogeneity-distorted image. We used the approach described in the “Exponential Signals With Spatially Smooth Parameters” section, which recovers the entire time series $\rho[\mathbf{r}, n]$ from the Fourier measurements. Postrecovery, the $\rho[\mathbf{r}, 0]$ image is chosen as the undistorted signal. Because there are two complex unknowns [i.e., $f(\mathbf{r})$ and $\beta(\mathbf{r})$], at each pixel, we use two shifted EPI readouts to recover the time series [29]. The results of this approach are shown in Figure 6(b).

Free-breathing, ungated cardiac MRI

In cardiac MRI clinical practice, breath-held cardiac cine MRI is the standard protocol to evaluate cardiac function (see Figure 8). Many subject groups cannot tolerate the breath holds, which disqualifies such patients for cardiac MRI exams. While free-breathing, ungated cardiac MRI is the ideal protocol, a main challenge is the significant acceleration needed to facilitate this scheme. The work in [21] used the surface recovery strategy discussed in the “Generalization to Machine Learning” section to recover free-breathing, ungated data from highly undersampled measurements with great success, as depicted in Figure 8(b).

Conclusions and future work

The SLR formulation provides a flexible framework to exploit different continuous-domain signal priors, which are difficult for current discrete compressive-sensing frameworks to capture. The framework comprises theoretical guarantees and fast algorithms and software, making it readily applicable to multidimensional imaging problems, including MRI. The recent results showed that there are important links between SLR frameworks and machine-learning approaches. The proposed framework is demonstrated in several challenging MRI applications. In spite of its flexibility and many applications, there remain open challenges, some of which are discussed next.

Sampling patterns

The single-channel theoretical results, i.e., (16) and (18), guarantee the recovery of the Fourier coefficients of the signals on a grid from a randomly chosen subset of coefficients. The results exhibit a \log^4 dependence on the final grid size, suggesting an increased sample demand with larger grid sizes. However, from the “FRI Theory for Piecewise, Smooth 1D Signals” and “Piecewise Smooth Signals In Higher Dimensions” sections, we note that once the null space is identified, the signal extrapolation to any grid size is possible from the low-frequency Fourier samples [10, Th. 1]. This strongly suggests a variable-density sampling approach, which may significantly reduce the sampling demand, and which was also confirmed by the empirical results in [16]. Additional theoretical work in this area is needed to determine the best sampling patterns.

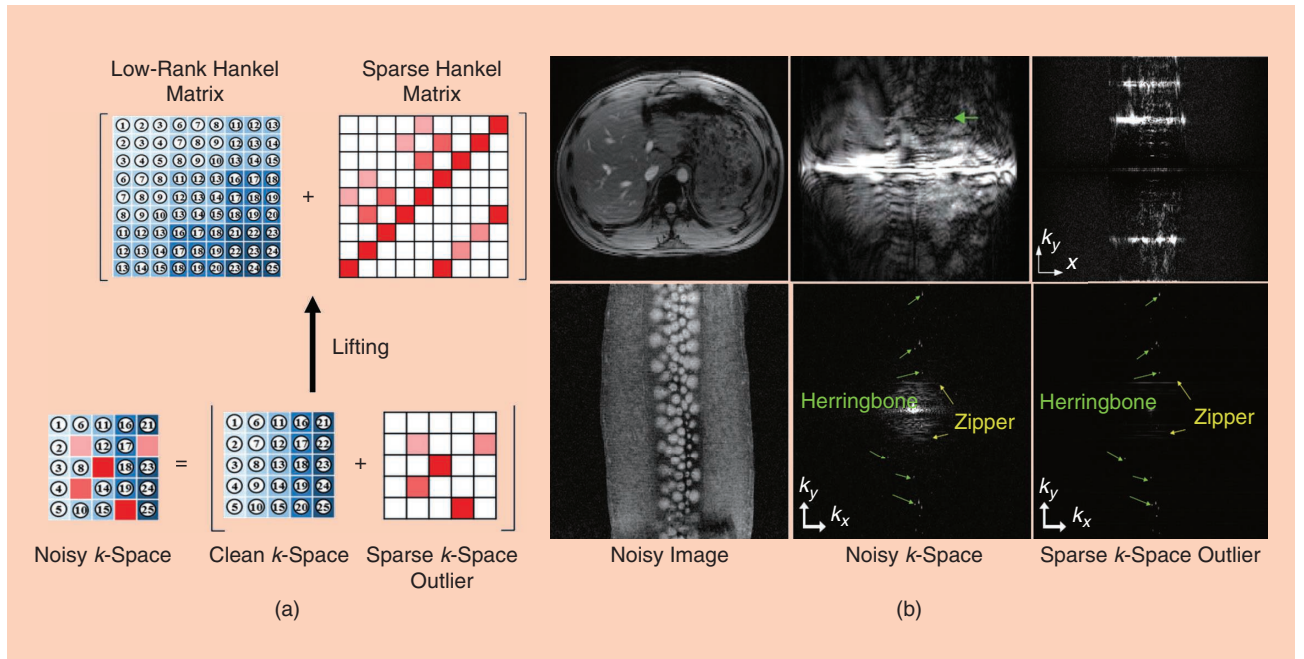


FIGURE 7. (a) The lifting of an image with a sparse outlier. The noiseless image becomes a low-rank Hankel matrix, whereas the noisy image becomes a sparse Hankel matrix so that robust principal component analysis can decompose the sparse and low-rank Hankel matrices. Then, by unlifting the Hankel matrix, we can obtain the noiseless k -space data and the clean images. (b) An example of MR artifact removals: (left) noisy images, (center), a noisy k -space, and (right) decomposed sparse k -space outliers. (Used with permission from [17].)

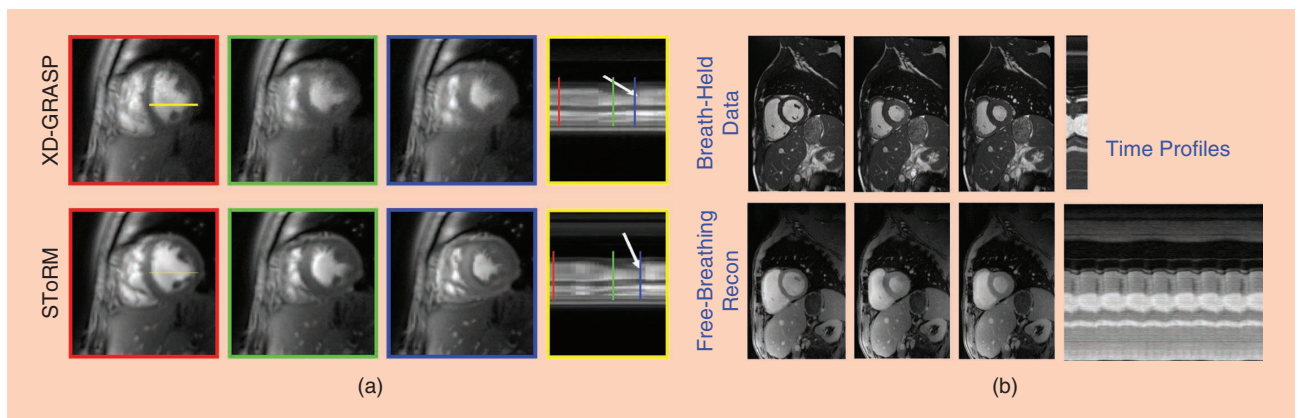


FIGURE 8. An illustration of the STORM algorithm [21] described in the “Free-Breathing, Ungated Cardiac MRI” section. The STORM algorithm exploits the manifold structure of free-breathing, ungated images in high-dimensional space. Specifically, each image can be viewed as a smooth function of two parameters: the cardiac phase and the respiratory phase. A nonlinear transformation specified by (29) transforms the data to a subspace. The STORM algorithm recovers the images from their undersampled measurements by exploiting this structure, which is compactly captured by nuclear norm of the feature matrix. The optimization problem is solved using an IRLS algorithm that uses the kernel trick, which eliminates the need to explicitly evaluate the complex features. (a) shows the comparisons of STORM reconstructed images with XD-GRASP, which is an explicit binning strategy; XD-GRASP bins the images to distinct cardiac/respiratory phases, followed by the total variation recovery of the images. Note that the implicit binning of the data offered by STORM results in reduced blurring and improved fidelity. (b) The comparisons of STORM reconstructions (bottom row) with classical breath-held acquisitions (top-row) that bins the data from different cardiac cycles. The image quality is noted to be comparable, while STORM offers real-time imaging capabilities, allowing to visualize cardiac and respiratory functions simultaneously.

Although empirical results demonstrate the great benefit of SLR schemes in multichannel signal recovery from nonuniform samples, this problem is not well studied from a theoretical perspective. However, the SLR framework can still be adapted to work well through the synergistic combination of multiple signal priors (e.g., sparsity and multichannel annihilation priors) achieved by composite lifting [18]. Additional theoretical work is needed on this front to improve the understanding of this problem.

Theoretical guarantees and noise performance

Most of the existing analysis assumes that the measurements are noise free and the underlying SLR matrix is low rank. For example, the multichannel annihilation relationship in (20) is valid only for the noiseless k -space measurements. The model mismatch introduces a slow decay of the singular value spectrum of the Hankel matrix. The aforementioned theoretical results are extended to scenarios involving measurement noise in specific SLR models in [14] and [16]. However, note that SLR formulations can be obtained from many different redundancies within the signal [5], [7], [18], [29]; the generalization of the theoretical robustness results in [14] and [16] to typical SLR schemes deserves further investigation.

Links between machine learning and SLR

Although the aforementioned link between SLR and deep learning is interesting, open questions remain and further theoretical work is necessary to understand this connection. The generalizability, optimization landscape, and expressivity (see the extensive list of references in [38]) in the context of machine-learning-based reconstruction are still not well understood, which may be an important research direction.

Acknowledgments

Jong Chul Ye's work was supported by the National Research Foundation of Korea grant NRF-2016R1A2B3008104. Mathews Jacob's work was supported by the National Institutes of Health under grants 1R01EB019961-01A1 and R01EB019961-02S1.

Authors

Mathews Jacob (mathews-jacob@uiowa.edu) received his Ph.D. degree from the Biomedical Imaging Group, EPFL, Lausanne, Switzerland, in 2003. He was a Beckman Postdoctoral Fellow at the University of Illinois at Urbana-Champaign from 2003 to 2006. He is currently a professor in the Department of Electrical and Computer Engineering and is heading the Computational Biomedical Imaging Group at the University of Iowa, Iowa City. His research interests include image reconstruction, analysis, and quantification in the context of magnetic resonance imaging. He received the CAREER Award from the National Science Foundation and the Research Scholar Award from the American Cancer Society. He currently serves as the associate editor of *IEEE Transactions on Medical Imaging* and *IEEE Transactions on Computational Imaging* and is the general chair of the 2020 IEEE International Symposium on Biomedical Imaging. He is a Senior Member of the IEEE.

Merry P. Mani (merry-mani@uiowa.edu) received her Ph.D. degree from the University of Rochester, New York, in 2014. She was a postdoctoral fellow at the Magnetic Resonance Research Facility, the University of Iowa, Iowa City, from 2014 to 2018, where she developed diffusion magnetic resonance imaging (MRI) techniques for ultra-high field imaging. She is currently an assistant professor in the Department of Radiology at the University of Iowa. Her research focuses on developing fast and efficient MRI

techniques to study neurological disorders, with a focus on diffusion-based microstructure imaging. She is a recipient of the Young Investigator Award from the Brain and Behavior Research Foundation.

Jong Chul Ye (jong.ye@kaist.ac.kr) is currently a professor in the Department of Bio/Brain Engineering and an adjunct professor in the Department of Mathematical Sciences at the Korea Advanced Institute of Science and Technology, Daejeon, South Korea. He serves as an associate editor of *IEEE Transactions on Medical Imaging*, a senior editor of *IEEE Signal Processing Magazine*, and a section editor of *BMC Biomedical Engineering*. He is the chair of the IEEE Signal Processing Society Technical Committee for Computational Imaging (2020–2021) and a general cochair (with Mathews Jacob) of the 2020 IEEE Symposium on Biomedical Imaging. His group was awarded first place at the 2009 Recon Challenge at the International Society for Magnetic Resonance in Medicine workshop and second place at the 2016 Low Dose CT Grand Challenge organized by the American Association of Physicists in Medicine. His research interests include machine learning and sparse recovery for various imaging reconstruction problems in X-ray computerized tomography, magnetic resonance imaging, optics, ultrasound, and so on. He is a Fellow of the IEEE.

References

- [1] M. Doneva, "Mathematical models for magnetic resonance imaging reconstruction: An overview of the approaches, problems, and future research areas," *IEEE Signal Process. Mag.*, vol. 37, no. 1, pp. 24–32, Jan. 2020. doi: 10.1109/MSP.2019.2936964.
- [2] H. Barkhuijsen, R. De Beer, W. M. M. J. Bovee, J. H. N. Creyghton, and D. Van Ormondt, "Application of linear prediction and singular value decomposition (LPSVD) to determine NMR frequencies and intensities from the FID," *Magn. Reson. Med.*, vol. 2, no. 1, pp. 86–89, 1985. doi: 10.1002/mrm.1910020111.
- [3] Z.-P. Liang, E. M. Haacke, and C. W. Thomas, "High-resolution inversion of finite Fourier transform data through a localised polynomial approximation," *Inverse Probl.*, vol. 5, no. 5, 1989. doi: 10.1088/0266-5611/5/5/011. [Online]. Available: <https://doi.org/10.1088/0266-5611/5/5/011>
- [4] J. Zhang, C. Liu, and M. E. Moseley, "Parallel reconstruction using null operations," *Magn. Reson. Med.*, vol. 66, no. 5, pp. 1241–1253, 2011.
- [5] P. J. Shin, P. E. Z. Larson, M. A. Ohliger, M. Elad, J. M. Pauly, D. B. Vigneron, and M. Lustig, "Calibrationless parallel imaging reconstruction based on structured low-rank matrix completion," *Magn. Reson. Med.*, vol. 72, no. 4, pp. 959–970, 2014.
- [6] M. Uecker, P. Lai, M. J. Murphy, P. Virtue, M. Elad, J. M. Pauly, S. Vasanawala, and M. Lustig, "ESPIRiT—an eigenvalue approach to autocalibrating parallel MRI: Where SENSE meets GRAPPA," *Magn. Reson. Med.*, vol. 71, no. 3, pp. 990–1001, 2014.
- [7] J. P. Haldar, "Low-rank modeling of local k -space neighborhoods (LORAKS) for constrained MRI," *IEEE Trans. Med. Imag.*, vol. 33, no. 3, pp. 668–681, 2014.
- [8] X. Qu, M. Mayzel, J.-F. Cai, Z. Chen, and V. Orekhov, "Accelerated NMR spectroscopy with low-rank reconstruction," *Appl. Chem.*, vol. 54, no. 3, pp. 852–854, 2015.
- [9] K. H. Jin, D. Lee, and J. C. Ye, "A general framework for compressed sensing and parallel MRI using annihilating filter based low-rank Hankel matrix," *IEEE Trans. Comput. Imag.*, vol. 2, no. 4, pp. 480–495, 2016.
- [10] G. Ongie and M. Jacob, "Off-the-grid recovery of piecewise constant images from few Fourier samples," *SIAM J. Imag. Sci.*, vol. 9, no. 3, pp. 1004–1041, 2016.
- [11] P. Cao, P. J. Shin, I. Park, C. Najac, I. Marco-Rius, D. B. Vigneron, S. J. Nelson, S. M. Ronen et al., "Accelerated high bandwidth MR spectroscopic imaging using compressed sensing," *Magn. Reson. Med.*, vol. 76, no. 2, pp. 369–379, 2016.
- [12] X. Peng, L. Ying, Y. Liu, J. Yuan, X. Liu, and D. Liang, "Accelerated exponential parameterization of T2 relaxation with model-driven low rank and sparsity priors (MORASA)," *Magn. Reson. Med.*, vol. 76, no. 6, pp. 1865–1878, 2016.
- [13] J. P. Haldar and J. Zhuo, "P-LORAKS: Low-rank modeling of local k -space neighborhoods with parallel imaging data," *Magn. Reson. Med.*, vol. 75, no. 4, pp. 1499–1514, 2016.
- [14] J. C. Ye, J. M. Kim, K. H. Jin, and K. Lee, "Compressive sampling using annihilating filter-based low-rank interpolation," *IEEE Trans. Inf. Theory*, vol. 63, no. 2, pp. 777–801, 2017.
- [15] G. Ongie and M. Jacob, "A fast algorithm for convolutional structured low-rank matrix recovery," *IEEE Trans. Comput. Imag.*, vol. 3, no. 4, pp. 535–550, 2017.
- [16] G. Ongie, S. Biswas, and M. Jacob, "Convex recovery of continuous domain piecewise constant images from nonuniform Fourier samples," *IEEE Trans. Signal Process.*, vol. 66, no. 1, pp. 236–250, 2018.
- [17] K. H. Jin, J.-Y. Um, D. Lee, J. Lee, S.-H. Park, and J. C. Ye, "MRI artifact correction using sparse + low-rank decomposition of annihilating filter-based Hankel matrix," *Magn. Reson. Med.*, vol. 78, no. 1, pp. 327–340, 2017.
- [18] M. Mani, M. Jacob, D. Kelley, and V. Magnotta, "Multi-shot sensitivity-encoded diffusion data recovery using structured low-rank matrix completion (MUSSELS)," *Magn. Reson. Med.*, vol. 78, no. 2, pp. 494–507, 2017.
- [19] B. Bilgic, T. H. Kim, C. Liao, M. K. Manhard, L. L. Wald, J. P. Haldar, and K. Setsompop, "Improving parallel imaging by jointly reconstructing multi-contrast data," *Magn. Reson. Med.*, vol. 80, no. 2, pp. 619–632, 2018.
- [20] Y. Hu, X. Liu, and M. Jacob, "A generalized structured low-rank matrix completion algorithm for MR image recovery," *IEEE Trans. Med. Imag.*, vol. 38, no. 8, pp. 1841–1851, 2018.
- [21] S. Poddar, Y. Mohsin, D. Ansah, B. Thattaliyath, R. Ashwath, and M. Jacob, "Free-breathing cardiac MRI using bandlimited manifold modelling," *IEEE Trans. Comput. Imag.*, vol. 35, no. 4, pp. 1106–1115, 2018.
- [22] J. P. Haldar and K. Setsompop, "Linear predictability in MRI reconstruction: Leveraging shift-invariant Fourier structure for faster and better imaging," *IEEE Signal Process. Mag.*, to be published.
- [23] E. Candes and C. Granda, "Towards a mathematical theory of super-resolution," *Pure Appl. Math.*, vol. 67, no. 6, pp. 906–956, 2014.
- [24] B. Scholkopf and A. J. Smola, *Learning With Kernels: Support Vector Machines, Regularization, Optimization, and Beyond*. Cambridge, MA: MIT Press, 2001.
- [25] M. Vetterli, P. Marziliano, and T. Blu, "Sampling signals with finite rate of innovation," *IEEE Trans. Signal Process.*, vol. 50, no. 6, pp. 1417–1428, 2002.
- [26] I. Dologlou, D. van Ormondt, and G. Carayannis, "MRI scan time reduction through non-uniform sampling and SVD-based estimation," *Signal Process.*, vol. 55, no. 2, pp. 207–219, 1996.
- [27] D. Guo, H. Lu, and X. Qu, "A fast low rank Hankel matrix factorization reconstruction method for non-uniformly sampled magnetic resonance spectroscopy," *IEEE Access*, vol. 5, pp. 16,033–16,039, July 2017.
- [28] H. Nguyen, B. Sutton, R. Morrison, and M. Do, "Joint estimation and correction of geometric distortions for EPI functional MRI using harmonic retrieval," *IEEE Trans. Med. Imag.*, vol. 28, no. 3, pp. 423–434, 2009.
- [29] A. Balachandrasekaran, M. Mani, and M. Jacob, "Calibration-free B0 correction of EPI data using structured low rank matrix recovery," *IEEE Trans. Med. Imag.*, vol. 38, no. 4, pp. 979–990, 2018.
- [30] E. Candes, J. Romberg, and T. Tao, "Robust uncertainty principles: Exact signal reconstruction from highly incomplete frequency information," *IEEE Trans. Inform. Theory*, vol. 52, no. 2, pp. 489–509, 2006.
- [31] H. Pan, T. Blu, and P. L. Dragotti, "Sampling curves with finite rate of innovation," *IEEE Trans. Signal Process.*, vol. 62, no. 2, pp. 458–471, 2014.
- [32] M. I. Gurelli and C. L. Nikias, "EVAM: An eigenvector-based algorithm for multichannel blind deconvolution of input colored signals," *IEEE Trans. Signal Process.*, vol. 43, no. 1, pp. 134–149, 1995.
- [33] M. A. Griswold, P. M. Jakob, R. M. Heidemann, M. Nittka, V. Jellus, J. Wang, B. Kiefer, and A. Haase, "Generalized autocalibrating partially parallel acquisitions (GRAPPA)," *Magn. Reson. Med.*, vol. 47, no. 6, pp. 1202–1210, 2002.
- [34] R. L. Morrison, M. Jacob, and M. N. Do, "Multichannel estimation of coil sensitivities in parallel MRI," in *Proc. IEEE Int. Symp. Biomedical Imaging*, 2007, pp. 117–120.
- [35] N. Srebro, "Learning with matrix factorizations," Ph.D. dissertation, Dept. Elect. Eng., Comput. Sci., Massachusetts Inst. Technol., Cambridge, MA, 2004.
- [36] K. Mohan and M. Fazel, "Iterative reweighted algorithms for matrix rank minimization," *J. Mach. Learn. Res.*, vol. 13, pp. 3441–3473, Nov. 2012.
- [37] J. Ye, Y. Han, and E. Cha, "Deep convolutional framelets: A general deep learning framework for inverse problems," *SIAM J. Imag. Sci.*, vol. 11, no. 2, pp. 991–1048, 2018.
- [38] J. C. Ye and W. K. Sung, "Understanding geometry of encoder-decoder CNNs," in *36th Int. Conf. Machine Learning, Ser. Proceedings of Machine Learning Research*, vol. 97, K. Chaudhuri and R. Salakhutdinov, Eds. Long Beach, CA: PMLR, 2019, pp. 7064–7073.
- [39] W. Jiang, P. E. Z. Larson, and M. Lustig, "Simultaneous auto-calibration and gradient delays estimation (SAGE) in non-Cartesian parallel MRI using low-rank constraints," *Magn. Reson. Med.*, vol. 80, no. 5, pp. 2006–2016, 2019.
- [40] M. Bydder, S. Rapacchi, O. Girard, M. Guye, and J.-P. Ranjeva, "Trimmed autocalibrating k -space estimation based on structured matrix completion," *Magn. Reson. Imag.*, vol. 43, no. 88, pp. 88–94, 2017.